








Bulk properties of the chiral metallic triangular antiferromagnets $\text{Ni}_{1/3}\text{NbS}_2$ and $\text{Ni}_{1/3}\text{TaS}_2$

Yeochan An ^{1,2}, Pyeongjae Park ^{1,2}, Chaebin Kim,^{1,2} Kaixuan Zhang ^{1,2}, Hyeoncheol Kim,^{1,2} Maxim Avdeev,^{3,4} Jaewon Kim ⁵, Myung-Joon Han,⁵ Han-Jin Noh,⁶ Seungho Seong ⁷, J.-S. Kang ⁷, Hyeong-Do Kim,⁸ and Je-Geun Park ^{1,2,*}

¹Center for Quantum Materials, Seoul National University, Seoul 08826, Republic of Korea

²Department of Physics and Astronomy, Seoul National University, Seoul 08826, Republic of Korea

³Australian Nuclear Science and Technology Organization, Locked Bag 2001, Kirrawee DC, NSW 2232, Australia


⁴School of Chemistry, The University of Sydney, Sydney, NSW 2006, Australia

⁵Department of Physics, KAIST, Daejeon 34141, Republic of Korea

⁶Department of Physics, Chonnam National University, Gwangju 61186, Republic of Korea

⁷Department of Physics, The Catholic University of Korea, Bucheon 14662, Republic of Korea

⁸PAL-XFEL, Pohang Accelerator Laboratory, Pohang, Gyeongbuk 37673, Republic of Korea

 (Received 3 February 2023; revised 21 June 2023; accepted 24 July 2023; published 11 August 2023)

$\text{TM}_{1/3}\text{MS}_2$ ($\text{TM} = 3d$ transition metal, $M = \text{Nb}, \text{Ta}$) has recently attracted increasing attention due to its wide variety of fascinating magnetic structures and the chiral arrangement of intercalated TM atoms. We investigated the bulk properties of $\text{Ni}_{1/3}\text{NbS}_2$ and $\text{Ni}_{1/3}\text{TaS}_2$ using magnetization, transport, heat capacity, powder neutron diffraction, and x-ray absorption spectroscopy. $\text{Ni}_{1/3}\text{NbS}_2$ undergoes a phase transition at 84 K, developing an antiferromagnetic helical order with a very long period along the c axis ($33c$). On the other hand, a simple A-type spin configuration was observed for $\text{Ni}_{1/3}\text{TaS}_2$ below 158 K, where the spins are aligned to the c axis. These magnetic structures, combined with lattice chirality and metallicity, can lead to various intriguing transport properties, making $\text{Ni}_{1/3}\text{NbS}_2$ and $\text{Ni}_{1/3}\text{TaS}_2$ promising material candidates for future studies on antiferromagnetic spintronics.

DOI: [10.1103/PhysRevB.108.054418](https://doi.org/10.1103/PhysRevB.108.054418)

I. INTRODUCTION

Layered magnetism is an exciting playground and has been explored over the past few decades for the studies of low-dimensional magnetism. More recently, the field has undergone a drastic turn of fortune as a new van der Waals (vdW) magnet was discovered in the form of TMPS_3 in 2016 [1–5], followed soon by the discovery of $\text{Cr}_2\text{Ge}_2\text{Te}_6$ [6] and CrI_3 [7]. This discovery allows one to realize proper two-dimensional magnetic systems and opens a new window of opportunities [8,9]. Numerous efforts have been made to expand the basis of the materials for more exotic ground states of layered magnetism.

Meanwhile, the intercalation of magnetic atoms into the van der Waals gap of layered materials can provide more diverse platforms than otherwise possible with the existing vdW magnets to study layered magnetism. In particular, $\text{TM}_{1/3}\text{MS}_2$ ($\text{TM} = 3d$ transition metal, $M = \text{Nb}, \text{Ta}$) has recently drawn much attention due to its wide range of fascinating magnetic structures and the chiral arrangement of intercalated TM atoms. In $\text{TM}_{1/3}\text{MS}_2$, transition-metal atoms intercalate into van der Waals gaps of $2H\text{-(Nb, Ta)S}_2$ [Fig. 1(a)] and form a triangular lattice. This results in the unit cell of the host material becoming a $\sqrt{3} \times \sqrt{3}$ superlattice. The intercalants become divalent (TM^{2+}) or trivalent (TM^{3+}) and thus host

localized magnetic moments, which are embedded in the sea of conduction electrons originating from the Ta- or Nb d bands of metallic $2H\text{-(Nb, Ta)S}_2$ [10–13]. A large distance between the TM ions ($\sim 5.7\text{\AA}$ between nearest neighbors) leaves the Ruderman-Kittel-Kasuya-Yosida mechanism as the only likely route for the exchange interaction.

The sign of this exchange interaction strongly depends on the choice of TM and M , which enables access to a wide variety of magnetic structures by studying $\text{TM}_{1/3}\text{MS}_2$ [10,11]. Moreover, the intercalated TM atoms offer chiral nature to magnetism by breaking the inversion symmetry [11,12]. The intercalation deforms the position of the neighboring sulfur and M atoms, leading to the noncentrosymmetric $P6_322$ space group [10,11,14]. The lack of an inversion center allows Dzyaloshinskii-Moriya interactions [15], crucial to producing fascinating magnetic structures with chiral nature, such as a helical order and even skyrmion [16,17]. Indeed, previous research has revealed several exotic magnetic behaviors in $\text{TM}_{1/3}\text{MS}_2$, such as chiral helimagnetic order and soliton lattice in $\text{Cr}_{1/3}\text{NbS}_2$ [14,18–20], Z_3 nematicity and exchange-bias effect in $\text{Fe}_{1/3}\text{NbS}_2$ [21,22], and the anomalous Hall effect in chiral antiferromagnets $\text{Co}_{1/3}\text{TaS}_2$ and $\text{Co}_{1/3}\text{NbS}_2$ [23,24]. In contrast to the extensive studies on $\text{TM}_{1/3}\text{MS}_2$ [25,26], $\text{Ni}_{1/3}\text{NbS}_2$ and $\text{Ni}_{1/3}\text{TaS}_2$ have been barely studied.

We have conducted a comprehensive study on the bulk properties of $\text{Ni}_{1/3}\text{NbS}_2$ and $\text{Ni}_{1/3}\text{TaS}_2$, including their magnetization, transport properties, heat capacity, powder neutron diffraction, and x-ray absorption spectroscopy (XAS) results.

*Corresponding author: jgpark10@snu.ac.kr

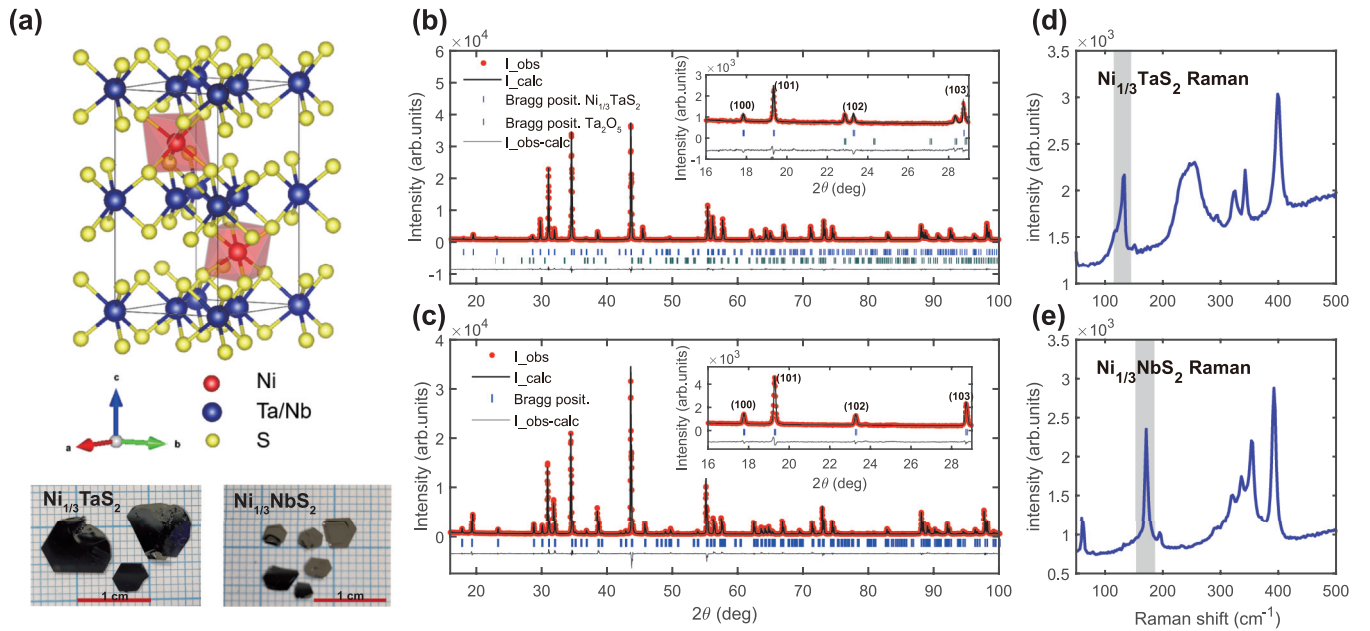


FIG. 1. Structural information of $\text{Ni}_{1/3}\text{TaS}_2$ and $\text{Ni}_{1/3}\text{NbS}_2$. (a) Crystal structure of $\text{Ni}_{1/3}\text{TaS}_2$ and $\text{Ni}_{1/3}\text{NbS}_2$. Image shows single crystals of $\text{Ni}_{1/3}\text{TaS}_2$ and $\text{Ni}_{1/3}\text{NbS}_2$. Red line in images represents 1 cm. Each sample has a size of 3 ~ 10 mm and a thickness of 100 ~ 200 μm . (b), (c) Powder XRD data and refinement results of $\text{Ni}_{1/3}\text{TaS}_2$ and $\text{Ni}_{1/3}\text{NbS}_2$. Inset shows superlattice peaks in XRD arising from Ni intercalation. (d), (e) Raman spectroscopy of single-crystal $\text{Ni}_{1/3}\text{TaS}_2$ and $\text{Ni}_{1/3}\text{NbS}_2$. Gray-shaded regions around 150 cm^{-1} indicate phonon mode highly relevant to intercalated Ni atoms.

Our analysis suggests that $\text{Ni}_{1/3}\text{NbS}_2$ forms helical order below 84 K while $\text{Ni}_{1/3}\text{TaS}_2$ becomes an *A*-type antiferromagnet with spins parallel to the *c* axis. Such a contrast in the magnetic structure is further investigated by magnetic anisotropy energy calculation by the density-functional theory (DFT) method. We also describe those magnetic structures based on minimal spin Hamiltonian.

II. EXPERIMENTAL METHODS

$\text{Ni}_{1/3}\text{NbS}_2$ and $\text{Ni}_{1/3}\text{TaS}_2$ crystals were grown by a two-step process. First, we synthesized polycrystalline $\text{Ni}_{1/3}\text{NbS}_2$ and $\text{Ni}_{1/3}\text{TaS}_2$ using the solid-state reaction method. A mixture of Ni (Alfa Aesar, >99.999%), Nb (Alfa Aesar, >99.99%), Ta (Sigma-Aldrich, >99.99%), and S (Sigma-Aldrich, >99.98%) powders in a molar ratio of 1.1:3:6 for $\text{Ni}_{1/3}\text{NbS}_2$ and 1.18:3:6 for $\text{Ni}_{1/3}\text{TaS}_2$ was ground in an Ar-filled glove box. The mixture was placed in an evacuated quartz ampoule and was sintered at 900 $^\circ\text{C}$ for 1 week. We performed powder x-ray diffraction (XRD) using a commercial high-resolution diffractometer (Smartlab, Rigaku, Japan) to check the resultant polycrystalline samples. Single crystals were grown from the prereacted polycrystals using the chemical vapor transport method with iodine as the transport agent (4.5 mg/cm^3). The samples were subject to a temperature gradient from 940 $^\circ\text{C}$ to 860 $^\circ\text{C}$ for 10 days. The resulting crystals are shiny hexagonal-shaped pieces as large as 3~10 mm with 100 ~ 200- μm thickness. We used energy-dispersive x-ray spectroscopy (EDX) to determine the composition of samples, which gives $\text{Ni}_{0.325(\pm 0.008)}\text{NbS}_2$ and $\text{Ni}_{0.338(\pm 0.002)}\text{TaS}_2$, close to the desired intercalation ratio (1/3). Raman spectroscopy (XperRam Compact, Nanobase

Korea) confirmed the high quality of the single-crystal samples.

Magnetization measurements were performed on the single-crystal samples using a commercial magnetometer (MPMS-XL5, Quantum Design USA). We measured transport properties using a standard four-probe method (CFMS9, Cryogenic Ltd UK). Specific heat was measured by using PPMS-14 (Quantum Design USA). We subtracted the nonmagnetic contribution of specific heat apart from its magnetic part. The nonmagnetic contribution was estimated by fitting the specific heat with a summation of electronic contribution ($\propto T$) and phonon contribution, where a combination of the Debye model and the Einstein model was used to model the latter contribution. The best-fitting results require two Debye temperatures ($\theta_{D1} = 260$ K, $\theta_{D2} = 545$ K) for $\text{Ni}_{1/3}\text{NbS}_2$ and one Debye temperature ($\theta_D = 205$ K) and two Einstein temperatures ($\theta_{E1} = 192$ K, $\theta_{E2} = 493$ K) for $\text{Ni}_{1/3}\text{TaS}_2$. In addition, the observed coefficient of electronic contribution (γ) is 11.6 $\text{mJ mol}^{-1} \text{K}^{-2}$ for $\text{Ni}_{1/3}\text{NbS}_2$, and 7 $\text{mJ mol}^{-1} \text{K}^{-2}$ for $\text{Ni}_{1/3}\text{TaS}_2$.

Powder neutron-diffraction data were collected using the Echidna high-resolution powder diffractometer [27] and the Wombat high-intensity powder diffractometer [28] at Australia's Nuclear Science and Technology Organisation. We analyzed the obtained data using the Rietveld refinement and group representation analysis using FULLPROF software [29]. The Ni L_2 - and L_3 -edge XAS measurements were held at the 2A beamline in Pohang Light Source, Korea.

We calculated total energy based on DFT implemented in the Vienna *Ab initio* Simulation Package (VASP) [30,31]. Generalized gradient approximation was adopted for the exchange-correlation functional as parametrized by Perdew, Burke, and Ernzerhof [32]. We used the projector

TABLE I. Crystallographic parameters of $\text{Ni}_{1/3}\text{TaS}_2$ with $P6_322$ space group (No. 182) obtained from Rietveld refinements on powder x-ray-diffraction data at room temperature.

$\text{Ni}_{1/3}\text{TaS}_2$		Space group: $P6_322$ (No. 182)			
		Cell dimensions: $a = b = 5.7352(1) \text{ \AA}$, $c = 11.9406(3) \text{ \AA}$, $\alpha = \beta = 90^\circ$, $\gamma = 120^\circ$			
Atom	Wyckoff position	x/a	y/b	z/c	Occupancy
Ta	$2a$	0	0	0	0.1667
Ta	$4f$	0.3333	0.6667	0.9983(6)	0.3333
Ni	$2c$	0.3333	0.6667	0.25	0.1629(4)
S	$12i$	0.6722(7)	0.0052(5)	0.1323(2)	1.023(35)
Agreement factors: $R_p(\%) = 7.59$, $R_{wp}(\%) = 7.04$, $R_{exp}(\%) = 5.82$, $X^2 = 1.46$					
Ta_2O_5 : 1.07 wt %					

augmented-wave potential [33] and the Γ -centered [34] k grid of $14 \times 14 \times 7$. The test calculations with the smaller number of k points give the same conclusion regarding the easy-axis directions. The energy cutoff was set at 600 eV with the convergence criterion of 10^{-7} eV, using the experimental lattice structure. The spin-orbit interaction was included in calculating the magnetic anisotropy energy in the relativistic noncollinear scheme. At the same time, the charge densities and the wave functions were acquired from the collinear spin calculations.

The classical Monte Carlo (MC) simulation was also performed to calculate the specific heat of our spin model, which yields the model's theoretical Néel temperature (T_N). We used the Metropolis-Hastings algorithm and simulated annealing for finite-temperature MC simulation. For $\text{Ni}_{1/3}\text{NbS}_2$, we sampled the total energy of a $16 \times 16 \times 66$ supercell with periodic boundary conditions over 200 000 MC steps after 1000 steps for equilibration. For $\text{Ni}_{1/3}\text{TaS}_2$, we used a $20 \times 20 \times 20$ supercell with periodic boundary conditions. The heat capacity (C_V) was subsequently calculated from a variance of the sampled total energy using the following equation:

$$C_V = \frac{\langle \epsilon^2 \rangle - \langle \epsilon \rangle^2}{k_B T^2}. \quad (1)$$

III. EXPERIMENTAL RESULTS AND ANALYSIS

A. Structural analysis

The formation of a noncentrosymmetric crystal structure ($P6_322$) and magnetism in $TM_{1/3}MS_2$ is attributed to the intercalants occupying the $2c$ Wyckoff sites. When intercalating into the host materials $2H\text{-NbS}_2/\text{TaS}_2$, a unit cell with a $\sqrt{3} \times \sqrt{3}$ superlattice is formed from the original host material. Additionally, structural chirality is induced by the clockwise or counterclockwise shifting of adjacent sulfur atom positions occupying $2c$ Wyckoff sites of the space group $P6_322$. However, the intercalation profile of transition-metal atoms can be easily disordered. Therefore, we carefully examined whether our samples had a correct intercalation profile without disorder using powder XRD and Raman spectroscopy. Figures 1(b) and 1(c) show the powder XRD patterns of polycrystalline $\text{Ni}_{1/3}(\text{Nb}, \text{Ta})\text{S}_2$, a precursor material to synthesize single crystals. Rietveld refinement of the XRD patterns confirmed that our sample had the same crystal structure as previously reported [12]. In particular, the Ni intercalation profile was

strictly verified by the $(10L)$ superlattice peaks located at the low-angle region of XRD data where L is an integer [Figs. 1(b) and 1(c), insets]. The refined occupancy of Ni intercalants from the XRD data (Tables I and II) further confirms the Ni composition close to $1/3$ with negligible vacancies, consistent with our EDX results. Sharp Raman peaks around 150 cm^{-1} for single-crystalline $\text{Ni}_{1/3}(\text{Nb}, \text{Ta})\text{S}_2$ [Figs. 1(d) and 1(e)] also confirmed a high quality of the Ni intercalation. Since the Raman peak around 150 cm^{-1} [shaded region in Figs. 1(d) and 1(e)] represents the phonon mode mainly driven by Ni in-plane vibrations, its peak sharpness is sensitive to the disorder in the Ni triangular lattice [35].

B. Magnetic property, electronic transport, and specific heat

As shown in Figs. 2(a) and 2(e), the magnetic susceptibility data of $\text{Ni}_{1/3}\text{TaS}_2$ and $\text{Ni}_{1/3}\text{NbS}_2$ show their antiferromagnetic character below the transition temperature at 158 and 84 K, respectively. Note that the transition temperature of $\text{Ni}_{1/3}\text{TaS}_2$ is much higher than that in previous bulk-properties research in the 1980s ($T_N = 125 \text{ K}$) [10–13]. The discrepancy may have occurred due to an enhanced sample quality with less Ni vacancy in our samples, as confirmed by XRD and Raman spectroscopy. Negative averaged Curie-Weiss temperatures ($\overline{\theta_{CW}} = \frac{1}{3}\theta_{CW}^{H\parallel c} + \frac{2}{3}\theta_{CW}^{H\perp c}$) are observed in $\text{Ni}_{1/3}\text{TaS}_2$ and $\text{Ni}_{1/3}\text{NbS}_2$ with the values of -41 and -109.6 K , respectively, indicating strong antiferromagnetic nature. Another interesting point is an unexpected difference in the magnetic anisotropy of $\text{Ni}_{1/3}\text{TaS}_2$ and $\text{Ni}_{1/3}\text{NbS}_2$: $\text{Ni}_{1/3}\text{TaS}_2$ has an easy axis parallel to the c axis. In contrast, $\text{Ni}_{1/3}\text{NbS}_2$ has an easy plane perpendicular to the c axis [Figs. 2(a) and 2(e)]. Although we briefly discuss the origin of such a difference, we think it is a subject for future theoretical studies.

Meanwhile, we observed the second phase transition around 80 K in the magnetization measurement of $\text{Ni}_{1/3}\text{TaS}_2$. The temperature dependence of magnetization in Fig. 2(a) shows a sudden jump in the magnetic susceptibility around 80 K, likely due to a weak ferromagnetic-like component. It is further demonstrated in the inset of Fig. 2(b); at $T = 10 \text{ K}$, a slight nonlinear behavior appears in the low-field region of the M - H curve.

The longitudinal resistivity of $\text{Ni}_{1/3}\text{TaS}_2$ and $\text{Ni}_{1/3}\text{NbS}_2$ are presented in Figs. 2(c) and 2(g), in which we observe a clear signature of the phase transition at 158 K for $\text{Ni}_{1/3}\text{TaS}_2$ and 84 K for $\text{Ni}_{1/3}\text{NbS}_2$, following our magnetic susceptibility data. However, no particular anomaly is observed around 80 K

TABLE II. Crystallographic parameters of $\text{Ni}_{1/3}\text{NbS}_2$ with $P6_322$ space group (No. 182) obtained from Rietveld refinements on powder x-ray-diffraction data at room temperature.

$\text{Ni}_{1/3}\text{NbS}_2$		Space group: $P6_322$ (No. 182)			
$T = 300\text{ K}$		Cell dimensions: $a = b = 5.7607(1)\text{ \AA}$, $c = 11.8964(3)\text{ \AA}$, $\alpha = \beta = 90^\circ$, $\gamma = 120^\circ$			
Atom	Wyckoff position	x/a	y/b	z/c	Occupancy
Nb	$2a$	0	0	0	0.1667
Nb	$4f$	0.3333	0.6667	0.9974(5)	0.3333
Ni	$2c$	0.3333	0.6667	0.25	0.1671(8)
S	$12i$	0.6682(3)	0.0006(9)	0.1328(0)	1.019(28)
Agreement factors: $R_p(\%) = 9.85$, $R_{wp}(\%) = 9.35$, $R_{exp}(\%) = 6.41$, $X^2 = 2.13$					

for $\text{Ni}_{1/3}\text{TaS}_2$, in contrast to the magnetic susceptibility data [Fig. 2(a)]. The major magnetic-phase transitions of the two compounds are also seen in the heat-capacity data [Figs. 2(d) and 2(h)] with a lambda-like peak (inset). In addition, the estimated magnetic moments' size from the integrated magnetic entropy gives effective spin for each Ni atom as $\frac{1}{2} < S < 1$, which has reduced spin compared to perfect localized Ni^{2+} systems, for both $\text{Ni}_{1/3}\text{TaS}_2$ and $\text{Ni}_{1/3}\text{NbS}_2$. Also, we remark that $\text{Ni}_{1/3}\text{NbS}_2$ exhibits a larger electronic contribution in conductivity and heat capacity than $\text{Ni}_{1/3}\text{TaS}_2$. This is evidenced by the electronic contribution in heat capacity (as described in Sec. II, Experimental Methods) and the conductivity.

C. Powder neutron-diffraction analysis and magnetic structure

Powder neutron diffraction was used to determine the magnetic structure of $\text{Ni}_{1/3}\text{TaS}_2$ and $\text{Ni}_{1/3}\text{NbS}_2$ (Fig. 3 and Tables III–V). Figure 3(b) demonstrates that the positions of the magnetic Bragg peaks in $\text{Ni}_{1/3}\text{TaS}_2$ at 3 K coincide precisely with those of nuclear Bragg peaks of (100), (101), and (102). It indicates that the magnetic propagation vector is $Q_m = (0, 0, 0)$. The spin configuration could be determined without ambiguity based on the irreducible representation analysis and Rietveld refinement [25,29]. While there are four possible irreducible representations (see also Table III) under the space group of

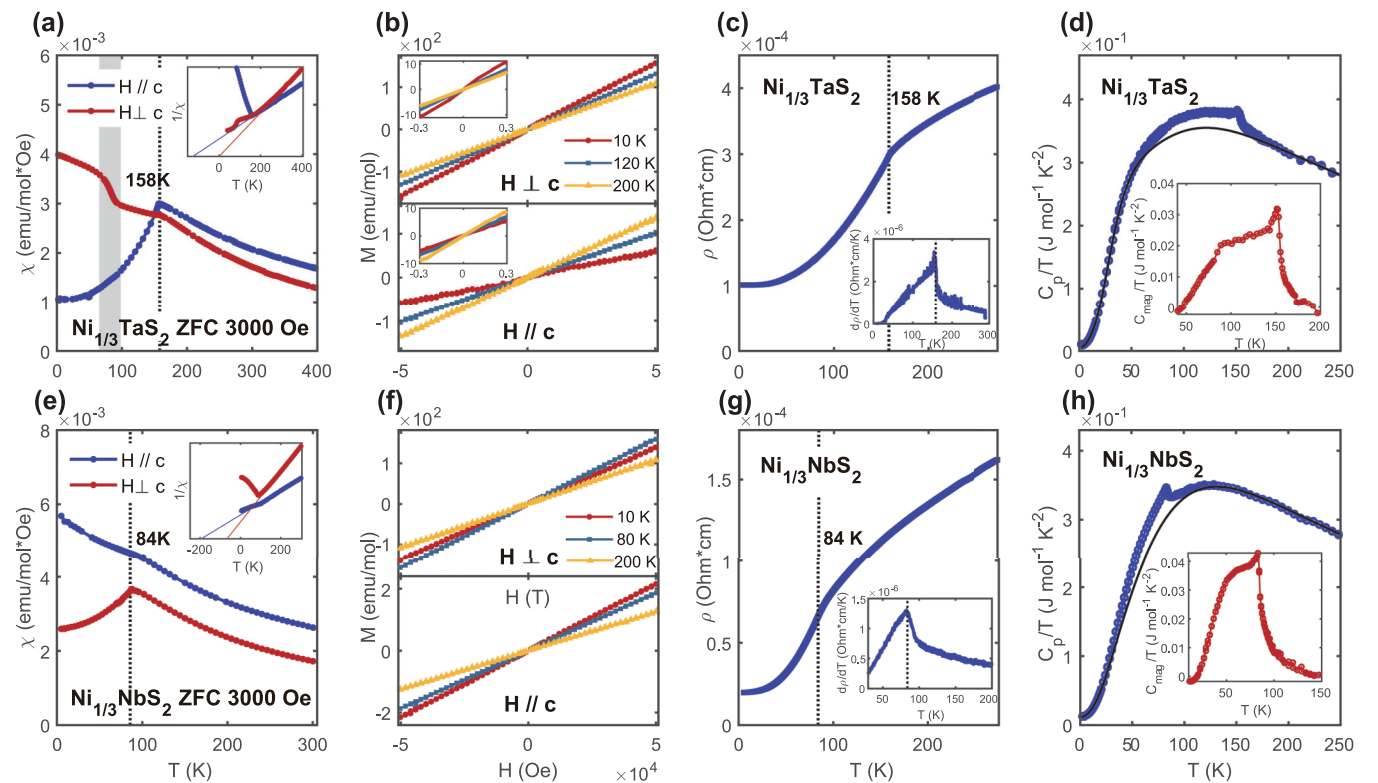


FIG. 2. Magnetic, transport, and thermodynamic properties of (a)–(d) $\text{Ni}_{1/3}\text{TaS}_2$ and (e)–(h) $\text{Ni}_{1/3}\text{NbS}_2$. (a) Temperature dependence of magnetic susceptibility per 1 mole of Ni measured with a field of 3 kOe applied parallel and perpendicular to c axis. Inset shows Curie-Weiss behavior. (b) $M(H)$ curves were obtained at three different temperatures. Insets in (b) show a low-field region for each $M(H)$ curve. (c) Temperature dependence of resistivity (ρ_{xx}). Inset shows temperature derivative of ρ_{xx} . (d) Heat capacity divided by temperature (C_p/T) and fitted nonmagnetic contributions of C_p/T (solid black line). Inset shows C_p/T related to magnetism derived by subtracting fitted nonmagnetic part from measured data. (e)–(h) Same as (a)–(d), but about $\text{Ni}_{1/3}\text{NbS}_2$.

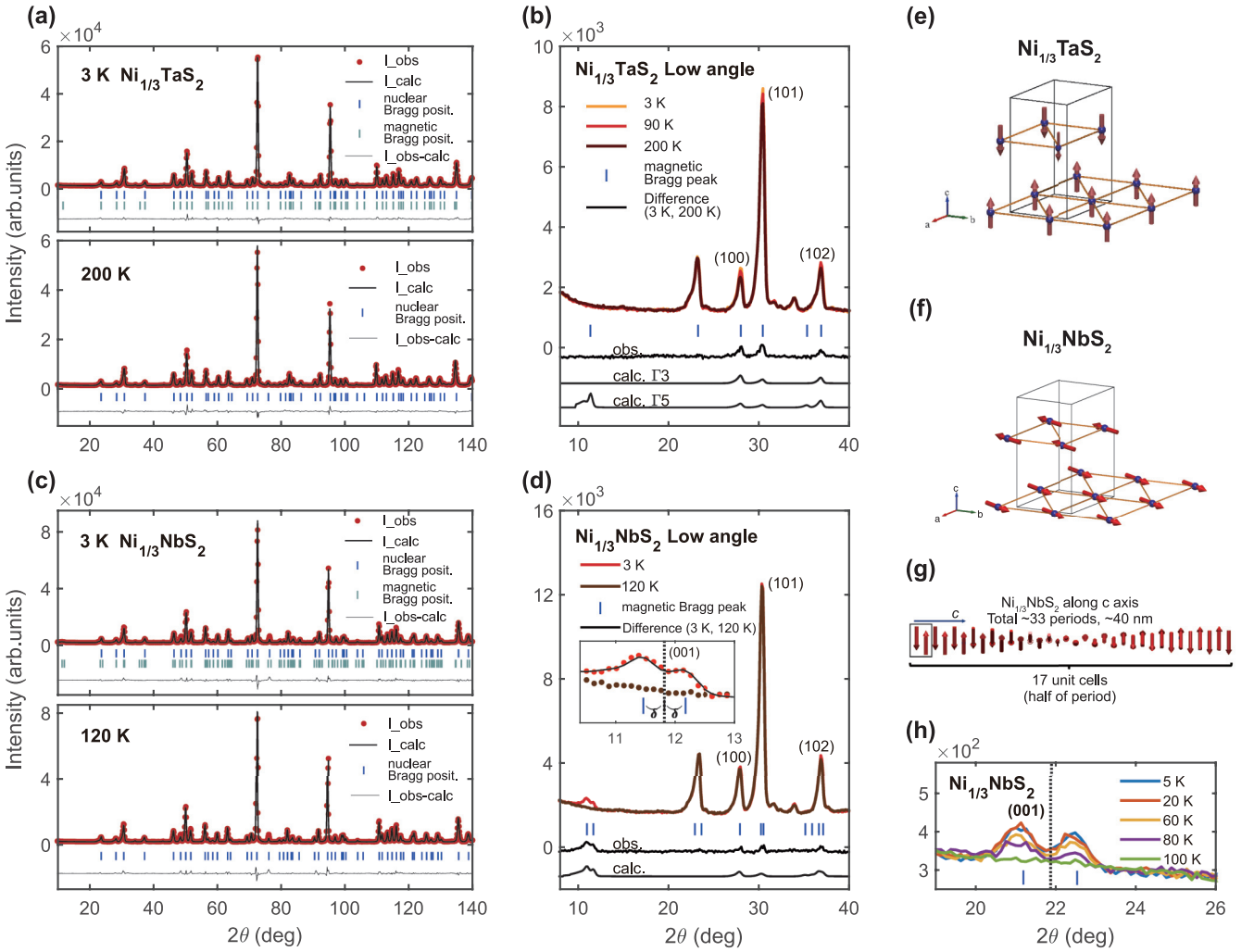


FIG. 3. (a) Refinement result of powder neutron-diffraction data of $\text{Ni}_{1/3}\text{TaS}_2$ for two temperature points, 3 and 200 K. (b) Low-angle region of (a). Difference between data measured at a temperature below and above phase transition (solid black lines) indicates magnetic signals. (c) Refinement result of powder neutron-diffraction data of $\text{Ni}_{1/3}\text{NbS}_2$ for two temperature points, 3 and 120 K. (d) Low-angle region of (c). Inset shows magnetic satellite peaks $(0, 0, 1 \pm \delta)$. (e), (f) Magnetic structures of (e) $\text{Ni}_{1/3}\text{TaS}_2$ and (f) $\text{Ni}_{1/3}\text{NbS}_2$. Blue spheres are Ni atoms, and red arrows indicate magnetic moment of each Ni atom. (g) Schematic magnetic structure of $\text{Ni}_{1/3}\text{NbS}_2$ along c axis with 17 unit cells is depicted, which is half period of helical order. (h) Temperature-dependent powder neutron-diffraction data of $\text{Ni}_{1/3}\text{NbS}_2$ near (001) . Note that measurements in (a)–(d) used a neutron beam with a wavelength of 2.4395 Å, and measurements in (h) used a wavelength of 4.74 Å.

TABLE III. Basis vectors of each irreducible representation for $\text{Ni}_{1/3}\text{TaS}_2$.

Irreducible representation	Type	Basis vector	Ni 1 (1/3, 2/3, 1/4)	Ni 2 (2/3, 1/3, 3/4)
Γ_1		\mathbf{v}_{11}		
Γ_2	FM ^a	\mathbf{v}_{21}	(0, 0, 1)	(0, 0, 1)
Γ_3	AFM ^b	\mathbf{v}_{31}	(0, 0, 1)	(0, 0, -1)
Γ_4		\mathbf{v}_{41}		
Γ_5	AFM	\mathbf{v}_{51}	$(0.612 - 0.354i, -0.707i, 0)$	$(-0.612 + 0.354i, 0.707i, 0)$
		\mathbf{v}_{52}	$(0.707i, -0.612 + 0.354i, 0)$	$(-0.707i, 0.612 - 0.354i, 0)$
Γ_6	FM	\mathbf{v}_{61}	$(0.612 - 0.354i, -0.707i, 0)$	$(0.612 - 0.354i, -0.707i, 0)$
		\mathbf{v}_{62}	$(-0.707i, 0.612 - 0.354i, 0)$	$(-0.707i, 0.612 - 0.354i, 0)$

^aFM = ferromagnetic.

^bAFM = antiferromagnetic.

TABLE IV. Parameters of $\text{Ni}_{1/3}\text{TaS}_2$ with space group $P6_322$ (No. 182) obtained from Rietveld refinements on powder neutron-diffraction data at 200 K, and magnetic R factor for two representations Γ_3 and Γ_5 at 3 K.

$\text{Ni}_{1/3}\text{TaS}_2$		Space group: $P6_322$ (No. 182)				
$T = 200$ K NPD		Cell dimensions: $a = b = 5.7272(4)$ Å, $c = 11.9205(5)$ Å, $\alpha = \beta = 90^\circ$, $\gamma = 120^\circ$				
Atom	Wyckoff position	x/a	y/b	z/c	$U_{\text{iso}}(\text{Å}^2)$	Occupancy
Ta	$2a$	0	0	0	0.2672(6)	0.166 67
Ta	$4f$	0.3333	0.6667	0.9978(0)	0.2175(5)	0.333 33
Ni	$2c$	0.3333	0.6667	0.25	0.8367(8)	0.165 9(2)
S	$12i$	0.6688(3)	0.0022(6)	0.1303(1)	0.3335(0)	0.990 8(6)
Agreement factors: $R_p(\%) = 10.7$, $R_{\text{wp}}(\%) = 11.7$, $R_{\text{exp}}(\%) = 3.47$, $X^2 = 11.2$						
Ta ₂ O ₅ : 1.00 wt. %						
$T = 3$ K		Γ_3 : $R_{\text{mag}}(\%) = 8.53$, Γ_5 : $R_{\text{mag}}(\%) = 14.1$				

$P6_322$ and $Q_m = (0, 0, 0)$, Γ_2 and Γ_6 should be excluded as they correspond to a ferromagnetic order. Between the possible antiferromagnetic representations Γ_3 (spins along the c axis) and Γ_5 (spins on the $a - b$ plane), Γ_3 is the only possible option since Γ_5 generates a strong (001) peak, in contrast to our experimental data with no (001) peak [Fig. 3(b)]. Therefore, the spin configuration of $\text{Ni}_{1/3}\text{TaS}_2$ is Γ_3 , an A -type antiferromagnet with spins aligned along the crystallographic c axis [Fig. 3(e)]. It is also consistent with our magnetic susceptibility data in Fig. 2(a) in that spins have an easy axis along the c axis. The best fit for the collected neutron powder-diffraction (NPD) data gives a magnetic moment of 1.03(0) and 0.95(5) μ_B at 3 and 90 K, respectively, similar to the size of the magnetic moment estimated by heat capacity. However, these values are much smaller than the ordered moment expected from Ni^{2+} under the ionic limit (2 μ_B). In addition, to understand the second phase transition of $\text{Ni}_{1/3}\text{TaS}_2$ around 80 K, we compared the magnetic signals obtained from the data at 90 K with the data at 3 K. However, there is no discernible change in the magnetic Bragg peaks' profile from our data, implying that the second transition is more subtle.

Figures 3(c) and 3(d) demonstrate the NPD patterns of $\text{Ni}_{1/3}\text{NbS}_2$ below (3 K) and above (120 K), the magnetic-phase transition. $\text{Ni}_{1/3}\text{NbS}_2$ shows the strongest magnetic

signal near (001), which is not a single peak but two satellite peaks equally split from the (001) position. This result indicates that the magnetic propagation vector of $Q_m = (0, 0, \delta)$ (reciprocal lattice units), which is the only case that can give two satellite peaks at $(0, 0, 1 \pm \delta)$ as observed in the data. As opposed to the case of $\text{Ni}_{1/3}\text{TaS}_2$, the out-of-plane spin component is ruled out by the presence of the strong $(0, 0, 1 \pm \delta)$ peak. Therefore, the spins should lie in a plane perpendicular to the c axis [Fig. 3(f)], again in agreement with the magnetic susceptibility data. The Rietveld refinement yields $\delta = 0.03$ with a magnetic moment of 1.05 μ_B , and therefore, the resulting magnetic structure is an antiferromagnetic helical order along the c axis with a long period of $33c$ [Figs. 3(f) and 3(g)]. Furthermore, the propagation vector of $\text{Ni}_{1/3}\text{NbS}_2$ is robust under the changes in temperature below the phase-transition temperature, as shown in Fig. 3(h).

We conducted further theoretical studies to understand the different anisotropic nature of $\text{Ni}_{1/3}\text{TaS}_2$ and $\text{Ni}_{1/3}\text{NbS}_2$. For example, we calculated the electronic band structure with two specific spin alignments (in plane, out of plane) and compared their total energies (Fig. 4). Our calculation implies $\text{Ni}_{1/3}\text{TaS}_2$ is more stable with the out-of-plane spin configuration than with the in-plane by 804.39 μeV per Ni atom. At the same time, $\text{Ni}_{1/3}\text{NbS}_2$ slightly prefers the in-plane spin configuration to the out of plane by 114.08 μeV per Ni

TABLE V. Parameters of $\text{Ni}_{1/3}\text{NbS}_2$ with space group $P6_322$ (No. 182) obtained from Rietveld refinements on powder neutron-diffraction data at 200 K, and magnetic R factor at 3 K.

$\text{Ni}_{1/3}\text{NbS}_2$		Space group: $P6_322$ (No. 182)				
$T = 120$ K NPD		Cell dimensions: $a = b = 5.7498(7)$ Å, $c = 11.8621(4)$ Å, $\alpha = \beta = 90^\circ$, $\gamma = 120^\circ$				
Atom	Wyckoff position	x/a	y/b	z/c	$U_{\text{iso}}(\text{Å}^2)$	Occupancy
Nb	$2a$	0	0	0	0.4259(6)	0.166 67
Nb	$4f$	0.3333	0.6667	0.9976(5)	0.3239(5)	0.333 33
Ni	$2c$	0.3333	0.6667	0.25	0.3816(2)	0.159 2(2)
S	$12i$	0.6680(1)	-0.0002(5)	0.1327(9)	0.1040(6)	0.919 4(9)
Agreement factors: $R_p(\%) = 11.3$, $R_{\text{wp}}(\%) = 13.3$, $R_{\text{exp}}(\%) = 2.69$, $X^2 = 24.5$						
$R_{\text{mag}}(\%) = 24.7$						
$T = 3$ K						

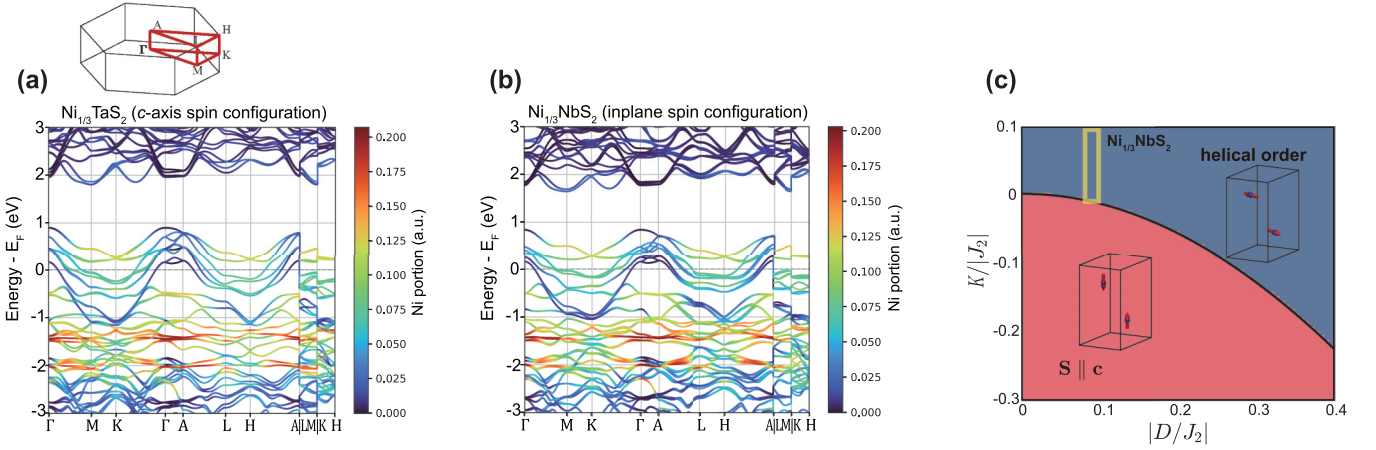


FIG. 4. (a), (b) Calculated band structure of (a) $\text{Ni}_{1/3}\text{TaS}_2$ with spin aligned to c axis (b) $\text{Ni}_{1/3}\text{NbS}_2$ with spin lying in a plane perpendicular to the c axis. Ni portions are depicted by color code. (c) Classical phase diagram of Hamiltonian equation (3) depending on parameters $|D/J_2|$ and $K/|J_2|$. Blue-colored phase represents an antiferromagnetic helical structure with a propagation vector of $(0, 0, \frac{\arctan(D/J_2)}{\pi})$. And, red color indicates structure with spins parallel to c axis. Solid black line is a phase boundary obtained by classical energy calculation. Yellow box shows expected position of $\text{Ni}_{1/3}\text{NbS}_2$ in parameter space.

atom. These magnetic anisotropy tendencies of $\text{Ni}_{1/3}\text{TaS}_2$ and $\text{Ni}_{1/3}\text{NbS}_2$ agree with the experimental results from magnetic susceptibility and powder neutron diffraction. We also include additional calculations in the appendixes with energy differences given for $\text{Ni}_{1/3}\text{Nb}_{1-x}\text{Ta}_x\text{S}_2$ (Appendix A) and the orbital occupation (Appendix B).

D. XAS analysis

Last, we studied the electronic state of Ni by Ni L -edge XAS, as shown in Fig. 5. When comparing the data with

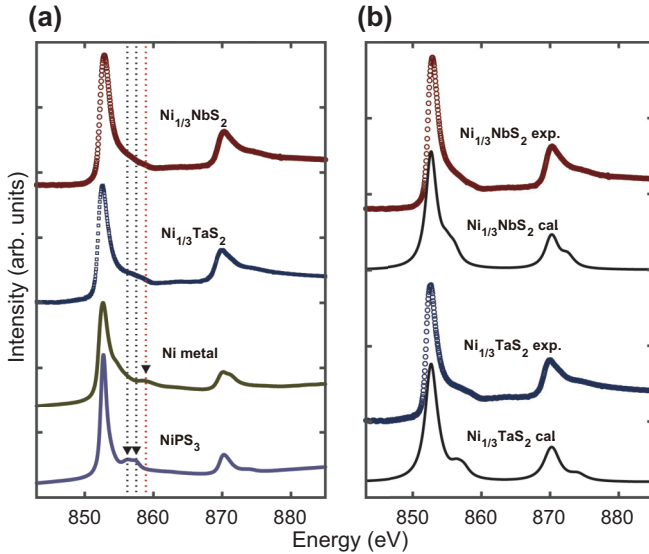


FIG. 5. Ni $L_{2,3}$ -edge XAS results of $\text{Ni}_{1/3}\text{TaS}_2$ and $\text{Ni}_{1/3}\text{NbS}_2$. (a) Comparison with XAS spectra of Ni metal and NiPS_3 . Dashed lines indicate characteristic energy spectrum of Ni metal (red dashed line) and NiPS_3 (black dashed line) to guide the eye for comparison. (b) Measured and calculated Ni $L_{2,3}$ -edge XAS spectra of $\text{Ni}_{1/3}\text{TaS}_2$ and $\text{Ni}_{1/3}\text{NbS}_2$.

those of Ni metal [Fig. 5(a)], we noticed that the shoulder spectra at the high-energy side of the L_3 edge (black dotted lines) are different from the Ni metal's feature (a red dotted line). Furthermore, we found these shoulder spectra somewhat resemble the XAS peak positions of NiPS_3 , which is known to contain significant effects of the sulfur ligands on Ni sites. Therefore, a possibility of the multiplet effect similar to NiPS_3 may be present in both $\text{Ni}_{1/3}\text{TaS}_2$ and $\text{Ni}_{1/3}\text{NbS}_2$ in terms of divalent Ni surrounded by octahedral sulfur atoms [36,37]. As shown in Fig. 5(b), we optimized six parameters to reproduce the experimental data based on the NiS_6 cluster calculation using QUANTY [38,39]: $10Dq$ is the cubic crystal-field parameter of $3d$ orbitals, U_{dd} and U_{pd} are Coulomb interactions by onsite $3d$ valence orbitals and between $3d$ valence and $2p$ core orbitals, V_{eg} and V_{2g} are the hopping integrals of σ - and π -type bonds between Ni $3d$ and S $3p$ orbitals, and Δ is charge-transfer energy from S $3p$ to Ni $3d$ states [38,39]. The best fit yields $10Dq = 1$ eV, $U_{dd} = 5$ eV, $U_{pd} = 6$ eV, $V_{eg} = 1$ eV, $V_{2g} = 0.6$ eV, and $\Delta = 1$ eV for $\text{Ni}_{1/3}\text{NbS}_2$, and $10Dq = 1$ eV, $U_{dd} = 5$ eV, $U_{pd} = 6$ eV, $V_{eg} = 1.8$ eV, $V_{2g} = 1$ eV, and $\Delta = 1$ eV for $\text{Ni}_{1/3}\text{TaS}_2$. Notably, these results indicate small charge-transfer energy ($\Delta \sim 1$ eV), as already demonstrated in systems with NiS_6 clusters [Fig. 5(b)] [40,41]. However, further interpretation of the electronic states is limited by the metallic nature of $\text{Ni}_{1/3}\text{TaS}_2$ and $\text{Ni}_{1/3}\text{NbS}_2$.

IV. DISCUSSION

We studied the bulk properties of $\text{Ni}_{1/3}\text{NbS}_2$ and $\text{Ni}_{1/3}\text{TaS}_2$ using several experimental techniques and theoretical calculations. These results reveal that the A -type antiferromagnetic configuration in $\text{Ni}_{1/3}\text{NbS}_2$ is stable below 84 K with moments perpendicular to the c axis and further contains the long-period helical order along the c axis. On the other hand, $\text{Ni}_{1/3}\text{TaS}_2$ forms an A -type antiferromagnetic order for $T < 158$ K, with spins pointing along the c axis.

TABLE VI. DFT-calculated orbital occupations for $\text{Ni}_{1/3}\text{MS}_2$ ($M = \text{Nb, Ta}$) based on which the noncollinear spin calculations were conducted. Atomic index 1 and 2 represent two distinct positions (atom 2 is located near Ni). Wigner-Seitz radius of each atom is as follows. Ni: 1.286 Å, Nb: 1.270 Å, Ta: 1.503 Å, and S: 1.164 Å.

$\text{Ni}_{1/3}\text{NbS}_2$						
Atom	Spin	Orbital				
		d_{xy}	$d_{yz/zx}$	d_{z^2}	$d_{x^2-y^2}$	d_{tot}
Ni	Up	1.03	1.01	0.96	1.03	5.04
	Down	0.89	0.77	0.92	0.90	4.25
	Diff	0.14	0.24	0.04	0.13	0.79
	Sum	1.92	1.78	1.88	1.93	9.29
Nb 1	Up	0.26	0.24	0.25	0.26	1.25
	Down	0.26	0.24	0.25	0.26	1.25
	Diff	0.00	0.00	0.00	0.00	0.00
	Sum	0.52	0.48	0.50	0.52	2.50
Nb 2	Up	0.26	0.25	0.24	0.25	0.26
	Down	0.25	0.25	0.24	0.25	0.25
	Diff	0.01	0.00	0.00	0.01	0.02
	Sum	0.51	0.50	0.48	0.51	2.50
S 1		P_x	P_y	P_z	P_{tot}	
	Up	0.42	0.41	0.43	1.26	
	Down	0.41	0.40	0.41	1.22	
	Diff	0.01	0.01	0.02	0.04	
S 2	Sum	0.83	0.81	0.84	2.48	
	Up	0.41	0.42	0.43	1.26	
	Down	0.4	0.42	0.41	1.23	
	Diff	0.01	0.00	0.02	0.03	
Sum	0.81	0.84	0.84	2.49		
$\text{Ni}_{1/3}\text{TaS}_2$						
Atom	spin	Orbital				
		d_{xy}	$d_{yz/zx}$	d_{z^2}	$d_{x^2-y^2}$	d_{tot}
Ni	Up	0.98	0.98	0.93	0.98	4.86
	Down	0.85	0.75	0.88	0.75	4.08
	Diff	0.13	0.23	0.05	0.23	0.78
	Sum	1.83	1.73	1.81	1.73	8.94
Ta 1	Up	0.25	0.25	0.23	0.25	1.23
	Down	0.25	0.25	0.23	0.25	1.23
	Diff	0.00	0.00	0.00	0.00	0.00
	Sum	0.50	0.50	0.46	0.50	2.46
Ta 2	Up	0.25	0.25	0.23	0.25	1.23
	Down	0.24	0.25	0.23	0.25	1.22
	Diff	0.01	0.00	0.00	0.00	0.01
	Sum	0.49	0.50	0.46	0.50	2.45
S 1		P_x	P_y	P_z	P_{tot}	
	Up	0.41	0.41	0.43	1.25	
	Down	0.41	0.40	0.41	1.22	
	Diff	0.00	0.01	0.02	0.03	
S 2	Sum	0.82	0.81	0.84	2.47	
	Up	0.40	0.42	0.43	1.25	
	Down	0.40	0.41	0.41	1.22	
	Diff	0.00	0.01	0.02	0.03	
Sum	0.80	0.83	0.84	2.47		

Here, we provide a short description of these magnetic ground states at the level of spin Hamiltonian. The simplest Hamiltonian that can explain the magnetic ground state of

$\text{Ni}_{1/3}\text{NbS}_2$ is

$$\hat{H} = \sum_{\langle i, j \rangle} J_1 \mathbf{S}_i \cdot \mathbf{S}_j + \sum_{\langle\langle i, j \rangle\rangle} J_2 \mathbf{S}_i \cdot \mathbf{S}_j + \sum_{\langle\langle i, j \rangle\rangle} \mathbf{D} \cdot (\mathbf{S}_i \times \mathbf{S}_j), \quad (2)$$

where the first (J_1) and the second (J_2) terms are, respectively, intralayer ($\langle i, j \rangle$) and interlayer ($\langle\langle i, j \rangle\rangle$) nearest neighbor (NN) exchange interactions and the third term describes the Dzyaloshinskii-Moriya (DM) interaction between interlayer NN with a DM vector \mathbf{D} [42,43]. Our magnetic structure requires that J_1 is ferromagnetic while J_2 is antiferromagnetic. Both the in-plane and out-of-plane components of \mathbf{D} are allowed by the symmetry of $\text{Ni}_{1/3}\text{NbS}_2$. However, the effect of three in-plane components of \mathbf{D} from three different interlayer NN bonds is eventually canceled out when a single Ni triangular layer is ferromagnetic [44]. Therefore, we can assume that \mathbf{D} is parallel to the c axis for simplicity. As well known, the out-of-plane component of \mathbf{D} causes interlayer-NN spin canting from parallel spin configuration, resulting in a helical structure along the c axis [44]. Furthermore, the out-of-plane component of \mathbf{D} naturally confines spins to the $a-b$ plane as it plays a role of effective easy-plane anisotropy. Treating \mathbf{S}_i as classical spin $\mathbf{S}_n = S e^{in\pi} (\cos \phi_n, \sin \phi_n, 0)$ with ϕ_n being a winding angle of the n th Ni triangular layer for the c axis, the ratio $|\mathbf{D}/J_2|$ can be determined from $\Delta\phi \equiv \phi_{n+1} - \phi_n$ [45]:

$$|\mathbf{D}/J_2| = \tan \Delta\phi. \quad (3)$$

In consequence, the experimental magnetic propagation vector of $\text{Ni}_{1/3}\text{NbS}_2$ ($Q_m = (0, 0, 0.03)$) necessitates the following value, $|\mathbf{D}/J_2| = 0.094$.

The magnetic ground states of $\text{Ni}_{1/3}\text{TaS}_2$ can be described by adding easy-axis anisotropy to Eq. (2),

$$\hat{H} = \sum_{\langle i, j \rangle} J_1 \mathbf{S}_i \cdot \mathbf{S}_j + \sum_{\langle\langle i, j \rangle\rangle} J_2 \mathbf{S}_i \cdot \mathbf{S}_j + \sum_{\langle\langle i, j \rangle\rangle} \mathbf{D} \cdot (\mathbf{S}_i \times \mathbf{S}_j) + K \sum_i (\mathbf{S}_i \cdot \hat{z})^2, \quad (4)$$

with $K < 0$. Unlike the case of $\text{Ni}_{1/3}\text{NbS}_2$, the spins in $\text{Ni}_{1/3}\text{TaS}_2$ neither form the helical order nor are perpendicular to the c axis. It implies that the effect of \mathbf{D} is suppressed somehow in $\text{Ni}_{1/3}\text{TaS}_2$ even though it is, in principle, allowed by the symmetry of the noncentrosymmetric $P6_322$ space group. Such suppression can be captured by including an easy-axis anisotropy to the Hamiltonian along the c axis, as far as it is large enough to overcome the effect of \mathbf{D} . To understand this effect, we investigated classical energy for both types of spin configurations. Each energy per site is

$$E_{\text{in}} = S^2(3J_1 + 3J_2 \cos \Delta\phi - 3|\mathbf{D}| \sin \Delta\phi), \quad (5)$$

$$E_c = S^2(3J_1 + 3J_2 + K), \quad (6)$$

and those give an analytic form of phase boundary from $E_{\text{in}} = E_c$ [solid black line in Fig. 4(c)]. Figure 4(c) shows a classical phase diagram for $|\mathbf{D}/J_2|$ and $K/|J_2|$, showing the competition between the in-plane helical order and out-of-plane spin configurations, each corresponding to the case of $\text{Ni}_{1/3}\text{NbS}_2$ and $\text{Ni}_{1/3}\text{TaS}_2$. At each point of the parameter space, the energy minimization algorithm was used to find a magnetic ground state, i.e., a relaxing magnetic structure. The phase diagram implies that even a small difference in parameters \mathbf{D} and K

can lead to a different state between the helical order and the out-of-plane spin configuration near the phase boundary.

A more quantitative analysis can derive a rough estimation of the Hamiltonian parameters. It was done by comparing the experimental Curie-Weiss temperature and the transition temperature (T_N) with those from mean-field approximation and classical Monte Carlo simulation (see Sec. II), respectively. We ignored the effect of \mathbf{D} and K on the Curie-Weiss temperature. As a result, we obtained $J_1 = -1.265$ meV and $J_2 = 3.626$ meV for $\text{Ni}_{1/3}\text{NbS}_2$, while $J_1 = -3.910$ meV and $J_2 = 4.793$ meV for $\text{Ni}_{1/3}\text{TaS}_2$. Subsequently, $|\mathbf{D}|$ can be determined to be 0.341 meV for $\text{Ni}_{1/3}\text{NbS}_2$. Although we cannot determine $|\mathbf{D}|$ and K in $\text{Ni}_{1/3}\text{TaS}_2$ precisely, we can roughly estimate their magnitude too. While $|\mathbf{D}|$ would be bigger in $\text{Ni}_{1/3}\text{TaS}_2$ because of the larger atomic number of Ta than Nb, the parameter K should be negative and can be an order of ~ 1 meV, as we confirmed using the DFT calculations. Consequently, we conclude that $\text{Ni}_{1/3}\text{NbS}_2$ is likely in the yellow box in the phase diagram [Fig. 4(c)], while $\text{Ni}_{1/3}\text{TaS}_2$ is located in the bottom-right region below the phase boundary.

We finally note that these magnetic structures, combined with lattice chirality and metallicity, can lead to various intriguing properties. It can enable the system to demonstrate exciting properties, including the chiral optical response [46,47] and the electrical magnetochiral anisotropy effect [48,49]. With magnetism introduced by intercalation, more opportunities will emerge in such a system for further fundamental research and device applications. For example, field-free electrical rectification may be achieved in $\text{Ni}_{1/3}\text{TaS}_2$ due to the spin aligning along the chiral axis. In addition, $\text{Ni}_{1/3}\text{NbS}_2$ is unique since it is the only case of quasi-two-dimensional helical antiferromagnetic metal, as far as we know, with the nearly collinear in-plane spin configuration of the A-type model. Such rare exotic spin texture with considerable Dzyaloshinskii-Moriya interaction can lead to chiral domain walls, skyrmions, and even antiferromagnetic switching by current excitation, enriching the chiral spintronics [50].

V. CONCLUSIONS

We measured the magnetization, transport, heat capacity, XAS, and powder neutron-diffraction spectra using high-quality $\text{Ni}_{1/3}\text{NbS}_2$ and $\text{Ni}_{1/3}\text{TaS}_2$ single crystals. These two compounds develop interesting but different magnetic structures: antiferromagnetic helical order with an extended period along the c axis ($33c$) for $\text{Ni}_{1/3}\text{NbS}_2$ and A-type antiferromagnet for $\text{Ni}_{1/3}\text{TaS}_2$. Notably, $\text{Ni}_{1/3}\text{NbS}_2$ and $\text{Ni}_{1/3}\text{TaS}_2$ show completely different magnetic anisotropy depending on the element of Nb and Ta, which is understood phenomenologically based on the spin Hamiltonian model and our DFT calculation. Our finding points to an exciting possibility of various intriguing transport properties in $\text{Ni}_{1/3}\text{NbS}_2$ and $\text{Ni}_{1/3}\text{TaS}_2$, making these two compounds promising material candidates for future studies on antiferromagnetic spintronics.

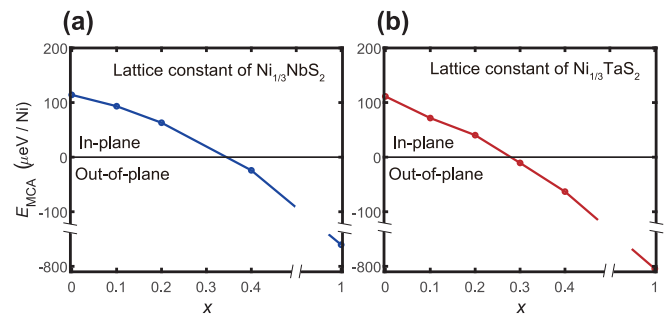


FIG. 6. Calculated total energy difference, $E_{\text{MCA}} (= E_{\text{out}} - E_{\text{in}})$, of $\text{Ni}_{1/3}\text{Nb}_{1-x}\text{Ta}_x\text{S}_2$ with lattice constants of (a) $\text{Ni}_{1/3}\text{NbS}_2$ and (b) $\text{Ni}_{1/3}\text{TaS}_2$ structures. E_{out} and E_{in} refers to total energy corresponding to magnetic moments being aligned along out-of-plane and in-plane (a -axis) direction, respectively. $x = 0.3$ point in (a) is omitted because of convergence issues.

ACKNOWLEDGMENTS

We thank Youjin Lee for valuable discussions. This work was supported by the Samsung Science & Technology Foundation (Grant No. SSTF-BA2101-05). J.-G.P. is partly funded by the Leading Researcher Program of the National Research Foundation of Korea (Grant No. 2020R1A3B2079375), and MSIT and POSTECH-supported experiments at PAL. J.-S.K. and S.S. acknowledge the support by the NRF (Grant No. 2019R1A2C1004929).

APPENDIX A: VIRTUAL CRYSTAL APPROXIMATION OF $\text{Ni}_{1/3}\text{Nb}_{1-x}\text{Ta}_x\text{S}_2$

Within virtual crystal approximation, we calculated the magnetocrystalline anisotropy (MCA) energy of $\text{Ni}_{1/3}\text{Nb}_{1-x}\text{Ta}_x\text{S}_2$ as a function of x . Note that the spin-orbit coupling (SOC) parameter (ζ) for Ta and Nb atoms is 2254–2643 and 646–748 cm^{-1} , respectively [51]. Two different structures of $\text{Ni}_{1/3}\text{NbS}_2$ [Fig. 6(a)] and $\text{Ni}_{1/3}\text{TaS}_2$ [Fig. 6(b)] were used in the calculations. Consistent with the result of the main text, the direction of the magnetic easy axis changes from in plane to out of plane as x increases. The small energy difference between the two lines reflects the structural effects of the anisotropy. Our results also imply that the magnetic dipole contribution (not contained in the current DFT scheme [52,53]) can hardly play a key role in determining the easy-axis direction of these materials.

APPENDIX B: THE CALCULATED ORBITAL OCCUPATIONS

Using the method discussed above, we calculated the electron occupations in each orbital and found its dependence on the type of M to be $\sim 10^{-2}$ (see Table VI).

- [1] C.-T. Kuo *et al.*, Exfoliation and Raman spectroscopic fingerprint of few-layer NiPS₃ van der Waals crystals, *Sci. Rep.* **6**, 20904 (2016).
- [2] C.-T. Kuo *et al.*, The energy band alignment at the interface between mechanically exfoliated few-layer NiPS₃ nanosheets and ZnO, *Curr. Appl. Phys.* **16**, 404 (2016).
- [3] S. Lee, K.-Y. Choi, S. Lee, B. H. Park, and J.-G. Park, Tunneling transport of mono- and few-layers magnetic van der Waals MnPS₃, *APL Mater.* **4**, 086108 (2016).
- [4] J.-U. Lee *et al.*, Ising-Type magnetic ordering in atomically thin FePS₃, *Nano Lett.* **16**, 7433 (2016).
- [5] K. Du *et al.*, Weak van der Waals stacking, wide-range band gap, and Raman study on ultrathin layers of metal phosphorus trichalcogenides, *ACS Nano* **10**, 1738 (2016).
- [6] C. Gong *et al.*, Discovery of intrinsic ferromagnetism in two-dimensional van der Waals crystals, *Nature (London)* **546**, 265 (2017).
- [7] B. Huang *et al.*, Layer-dependent ferromagnetism in a van der Waals crystal down to the monolayer limit, *Nature (London)* **546**, 270 (2017).
- [8] J.-G. Park, Opportunities and challenges of 2D magnetic van der Waals materials: Magnetic graphene?, *J. Phys.: Condens. Matter* **28**, 301001 (2016).
- [9] K. S. Burch, D. Mandrus, and J.-G. Park, Magnetism in two-dimensional van der Waals materials, *Nature (London)* **563**, 47 (2018).
- [10] S. S. P. Parkin and R. H. Friend, 3d transition-metal intercalates of the niobium and tantalum dichalcogenides. II. Transport properties, *Philos. Mag. B* **41**, 95 (1980).
- [11] S. S. P. Parkin and R. H. Friend, 3d transition-metal intercalates of the niobium and tantalum dichalcogenides. I. Magnetic properties, *Philos. Mag. B* **41**, 65 (1980).
- [12] B. Van Laar, H. M. Rietveld, and D. J. W. IJdo, Magnetic and crystallographic structures of Me_xNbS₂ and Me_xTaS₂, *J. Solid State Chem.* **3**, 154 (1971).
- [13] R. H. Friend, A. R. Beal, and A. D. Yoffe, Electrical and magnetic properties of some first row transition metal intercalates of niobium disulphide, *Philos. Mag.: J. Theor. Exp. Appl. Phys.* **35**, 1269 (1977).
- [14] K. Du *et al.*, Topological spin/structure couplings in layered chiral magnet Cr_{1/3}TaS₂: The discovery of spiral magnetic superstructure, *Proc. Natl. Acad. Sci.* **118**, e2023337118 (2021).
- [15] T. Moriya, New Mechanism of Anisotropic Superexchange Interaction, *Phys. Rev. Lett.* **4**, 228 (1960).
- [16] T. Moriya and T. Miyadai, Evidence for the helical spin structure due to antisymmetric exchange interaction in Cr_{1/3}NbS₂, *Solid State Commun.* **42**, 209 (1982).
- [17] U. K. Röbler, A. N. Bogdanov, and C. Pfleiderer, Spontaneous skyrmion ground states in magnetic metals, *Nature (London)* **442**, 797 (2006).
- [18] Y. Cao *et al.*, Overview and advances in a layered chiral helimagnet Cr_{1/3}NbS₂, *Mater. Today Adv.* **7**, 100080 (2020).
- [19] Y. Togawa *et al.*, Chiral Magnetic Soliton Lattice on a Chiral Helimagnet, *Phys. Rev. Lett.* **108**, 107202 (2012).
- [20] B. J. Chapman, A. C. Bornstein, N. J. Ghimire, D. Mandrus, and M. Lee, Spin structure of the anisotropic helimagnet Cr_{1/3}NbS₂ in a magnetic field, *Appl. Phys. Lett.* **105**, 072405 (2014).
- [21] A. Little *et al.*, Three-state nematicity in the triangular lattice antiferromagnet Fe_{1/3}NbS₂, *Nat. Mater.* **19**, 1062 (2020).
- [22] N. L. Nair *et al.*, Electrical switching in a magnetically intercalated transition metal dichalcogenide, *Nat. Mater.* **19**, 153 (2020).
- [23] N. J. Ghimire *et al.*, Large anomalous Hall effect in the chiral-lattice antiferromagnet CoNb₃S₆, *Nat. Commun.* **9**, 3280 (2018).
- [24] P. Park *et al.*, Field-tunable toroidal moment and anomalous Hall effect in noncollinear antiferromagnetic Weyl semimetal Co_{1/3}TaS₂, *npj Quantum Mater.* **7**, 42 (2022).
- [25] K. Lu, D. Sapkota, L. DeBeer-Schmitt, Y. Wu, H. B. Cao, N. Mannella, D. Mandrus, A. A. Aczel, and G. J. MacDougall, Canted antiferromagnetic order in the monoaxial chiral magnets V_{1/3}TaS₂ and V_{1/3}NbS₂, *Phys. Rev. Mater.* **4**, 054416 (2020).
- [26] H. Zhang *et al.*, Electrical and anisotropic magnetic properties in layered Mn_{1/3}TaS₂ crystals, *Appl. Phys. Lett.* **113**, 072402 (2018).
- [27] M. Avdeev and J. R. Hester, ECHIDNA: A decade of high-resolution neutron powder diffraction at OPAL, *J. Appl. Crystallogr.* **51**, 1597 (2018).
- [28] A. J. Studer, M. E. Hagen, and T. J. Noakes, Wombat: The high-intensity powder diffractometer at the OPAL reactor, *Physica B: Condens. Matter* **385–386**, 1013 (2006).
- [29] J. Rodríguez-Carvajal, Recent advances in magnetic structure determination by neutron powder diffraction, *Physica B: Condens. Matter* **192**, 55 (1993).
- [30] G. Kresse and J. Furthmüller, Efficiency of ab-initio total energy calculations for metals and semiconductors using a plane-wave basis set, *Comput. Mater. Sci.* **6**, 15 (1996).
- [31] G. Kresse and J. Furthmüller, Efficient iterative schemes for *ab initio* total-energy calculations using a plane-wave basis set, *Phys. Rev. B* **54**, 11169 (1996).
- [32] J. P. Perdew, K. Burke, and M. Ernzerhof, Generalized Gradient Approximation Made Simple, *Phys. Rev. Lett.* **77**, 3865 (1996).
- [33] P. E. Blöchl, Projector augmented-wave method, *Phys. Rev. B* **50**, 17953 (1994).
- [34] H. J. Monkhorst and J. D. Pack, Special points for Brillouin-zone integrations, *Phys. Rev. B* **13**, 5188 (1976).
- [35] S. Fan *et al.*, Excitations of intercalated metal monolayers in transition metal dichalcogenides, *Nano Lett.* **21**, 99 (2021).
- [36] K. Takubo, T. Mizokawa, J.-Y. Son, Y. Nambu, S. Nakatsuji, and Y. Maeno, Unusual Superexchange Pathways in an NiS₂ Triangular Lattice with Negative Charge-Transfer Energy, *Phys. Rev. Lett.* **99**, 037203 (2007).
- [37] S. Y. Kim, T. Y. Kim, L. J. Sandilands, S. Sinn, M.-C. Lee, J. Son, S. Lee, K.-Y. Choi, W. Kim, and B.-G. Park, Charge-Spin Correlation in van der Waals Antiferromagnet NiPS₃, *Phys. Rev. Lett.* **120**, 136402 (2018).
- [38] M. W. Haverkort, M. Zwierzycki, and O. K. Andersen, Multiplet ligand-field theory using Wannier orbitals, *Phys. Rev. B* **85**, 165113 (2012).
- [39] M. W. Haverkort, *Quanta* for core level spectroscopy - excitons, resonances and band excitations in time and frequency domain, *J. Phys. Conf. Ser.* **712**, 012001 (2016).
- [40] G. Shibata *et al.*, Large orbital magnetic moment and strong perpendicular magnetic anisotropy in heavily intercalated Fe_xTiS₂, *J. Phys. Chem. C* **125**, 12929 (2021).

- [41] J. Jeong *et al.*, Electronic structure change of $\text{NiS}_{2-x}\text{Se}_x$ in the metal-insulator transition probed by X-ray absorption spectroscopy, *J. Korean Phys. Soc.* **72**, 111 (2018).
- [42] S. Mankovsky, S. Polesya, H. Ebert, and W. Bensch, Electronic and magnetic properties of $2H\text{-NbS}_2$ intercalated by $3d$ transition metals, *Phys. Rev. B* **94**, 184430 (2016).
- [43] J. Kishine, K. Inoue, and K. Kikuchi, Static and dynamical anomalies caused by chiral soliton lattice in molecular-based chiral magnets, *J. Magn. Magn. Mater.* **310**, 1386 (2007).
- [44] D. Braam, C. Gomez, S. Tezok, E. V. L. de Mello, L. Li, D. Mandrus, H.-Y. Kee, and J. E. Sonier, Magnetic properties of the helimagnet $\text{Cr}_{1/3}\text{NbS}_2$ observed by μSR , *Phys. Rev. B* **91**, 144407 (2015).
- [45] A. A. Aczel *et al.*, Extended exchange interactions stabilize long-period magnetic structures in $\text{Cr}_{1/3}\text{NbS}_2$, *Appl. Phys. Lett.* **113**, 032404 (2018).
- [46] Y. Cui, L. Kang, S. Lan, S. Rodrigues, and W. Cai, Giant chiral optical response from a twisted-arc metamaterial, *Nano Lett.* **14**, 1021 (2014).
- [47] M. Hentschel, M. Schäferling, X. Duan, H. Giessen, and N. Liu, Chiral plasmonics, *Sci. Adv.* **3**, e1602735 (2017).
- [48] G. L. J. A. Rikken, J. Fölling, and P. Wyder, Electrical Magneto-chiral Anisotropy, *Phys. Rev. Lett.* **87**, 236602 (2001).
- [49] F. Pop, P. Auban-Senzier, E. Canadell, G. L. J. A. Rikken, and N. Avarvari, Electrical magneto-chiral anisotropy in a bulk chiral molecular conductor, *Nat. Commun.* **5**, 3757 (2014).
- [50] S.-H. Yang, R. Naaman, Y. Paltiel, and S. S. P. Parkin, Chiral spintronics, *Nat. Rev. Phys.* **3**, 328 (2021).
- [51] J. Bendix, M. Brorson, and C. E. Schaffer, Accurate empirical spin-orbit coupling parameters ζ_{nd} for gaseous nd^q transition metal ions. The parametrical multiplet term model, *Inorg. Chem.* **32**, 2838 (1993).
- [52] H. J. F. Jansen, Magnetic anisotropy in density-functional theory, *Phys. Rev. B* **38**, 8022 (1988).
- [53] C. Pellegrini, T. Müller, J. K. Dewhurst, S. Sharma, A. Sanna, and E. K. U. Gross, Density functional theory of magnetic dipolar interactions, *Phys. Rev. B* **101**, 144401 (2020).